

## Large-scale controls on extreme precipitation

Loriaux, Jessica M.; Lenderink, Geert; Siebesma, A.P.

**DOI**

[10.1175/JCLI-D-16-0381.1](https://doi.org/10.1175/JCLI-D-16-0381.1)

**Publication date**

2017

**Document Version**

Final published version

**Published in**

Journal of Climate

**Citation (APA)**

Loriaux, J. M., Lenderink, G., & Siebesma, A. P. (2017). Large-scale controls on extreme precipitation. *Journal of Climate*, 30(3), 955-968. <https://doi.org/10.1175/JCLI-D-16-0381.1>

**Important note**

To cite this publication, please use the final published version (if applicable). Please check the document version above.

**Copyright**

Other than for strictly personal use, it is not permitted to download, forward or distribute the text or part of it, without the consent of the author(s) and/or copyright holder(s), unless the work is under an open content license such as Creative Commons.

**Takedown policy**

Please contact us and provide details if you believe this document breaches copyrights. We will remove access to the work immediately and investigate your claim.

# Large-Scale Controls on Extreme Precipitation

JESSICA M. LORIAUX

*Delft University of Technology, Delft, and Royal Netherlands Meteorological Institute, De Bilt, Netherlands*

GEERT LENDERINK

*Royal Netherlands Meteorological Institute, De Bilt, Netherlands*

A. PIER SIEBESMA

*Delft University of Technology, Delft, and Royal Netherlands Meteorological Institute, De Bilt, Netherlands*

(Manuscript received 12 May 2016, in final form 3 October 2016)

## ABSTRACT

Large-eddy simulations with strong lateral forcing representative of precipitation over the Netherlands are performed to investigate the influence of stability, relative humidity (RH), and moisture convergence on precipitation. Furthermore, a simple climate perturbation is applied to analyze the precipitation response to increasing temperatures. Precipitation is decomposed to distinguish between processes affecting the precipitating area and the precipitation intensity. It is shown that amplification of the moisture convergence and destabilization of the atmosphere both lead to an increase in precipitation, but on account of different effects: atmospheric stability mainly influences the precipitation intensity, whereas the moisture convergence mainly controls the precipitation area fraction. Extreme precipitation intensities show qualitatively similar sensitivities to atmospheric stability and moisture convergence. Precipitation increases with RH due to an increase in area fraction, despite a decrease in intensity. The precipitation response to the climate perturbation shows a stronger response for the precipitation intensity than the overall precipitation, with no clear dependency on changes in atmospheric stability, moisture convergence, and relative humidity.

## 1. Introduction

In view of the disruptive nature of precipitation extremes to society, many studies have been published on the behavior of extreme precipitation and its response to climate change (O’Gorman 2015; Westra et al. 2014). Model predictions indicate that extreme precipitation will intensify and become more frequent with warming (IPCC 2014), and studies have already been able to attribute changes in extreme precipitation to observed warming (Min et al. 2011; Pall et al. 2011; Lenderink and Attema 2015). However, the magnitude of the response is quite variable (e.g., O’Gorman 2012) and the sensitivity of the response to mesoscale conditions is not yet completely understood in either present-day or future climate.

Present-day relations between observed temperature and precipitation extremes show an increase of approximately  $7\%–14\% K^{-1}$ , depending on the surface temperature, over western Europe (Lenderink and Meijgaard 2008; Lenderink and van Meijgaard 2010; Berg et al. 2013; Blenkinsop et al. 2015). Similar results were found for stations across Australia (Hardwick-Jones et al. 2010) and the United States (Mishra et al. 2012). Since these observed sensitivities of extreme precipitation may not necessarily translate to a response to global warming (Westra et al. 2014), it is important to understand the physical processes that influence extreme precipitation as well as the precipitation response.

The moisture holding capacity of the atmosphere increases with temperature. In areas where enough moisture is available, the specific humidity of the atmosphere will increase following the Clausius–Clapeyron (CC) equation. Near the surface, this amounts to an increase of approximately  $6\%–7\% K^{-1}$  (CC scaling). If

---

Corresponding author e-mail: Jessica M. Loriaux, jmloriaux@gmail.com

thermodynamics are dominant in determining extreme precipitation intensities, they are expected to increase at the same rate (Allen and Ingram 2002). However, precipitation extremes can be invigorated or diminished by dynamical processes (Trenberth et al. 2003; Emori and Brown 2005) and microphysics (Singh and O’Gorman 2014). These components are conceptualized in the following approximation of the precipitation rate:

$$P \approx -\varepsilon \int_{z_b}^{z_t} w_c \frac{\partial q_{s,c}}{\partial z} \rho dz. \quad (1)$$

This equation simply states that the precipitation rate  $P$  is determined by a precipitation efficiency  $\varepsilon$  times the vertically integrated condensation rate in the cloud. The condensation rate consists of a dynamic and thermodynamic contribution through the updraft velocity  $w_c$  and the vertical derivative of the saturation specific humidity following the parcel, namely  $q_{s,c}$ , respectively. If the updraft velocity and efficiency are constant with warming, for deep convection the precipitation response leads to CC scaling.

Analysis of the precipitation response to climate change in terms of Eq. (1) has been presented in numerous studies, using general circulation models (O’Gorman and Schneider 2009a,b), cloud-resolving models (Muller et al. 2011; Romps 2011; Muller 2013; Singh and O’Gorman 2015), and a conceptual model (Loriaux et al. 2013). While the thermodynamic component is understood quite well, the other components remain rather difficult to predict.

The influence of large-scale dynamics and environmental conditions on extreme precipitation, which indirectly influences the different components of (1), is not yet understood well enough. Combining observations and reanalysis data, Davies et al. (2013) studied the relations between large-scale moisture convergence, stability parameters, and tropical precipitation, finding that convective precipitation has a strong relationship with the large-scale vertical velocity and moisture convergence. Another study has analyzed circulation and several atmospheric conditions in relation to midlatitude peak precipitation (Loriaux et al. 2016b), finding only weak relationships with atmospheric stability and vertical velocity. Here, we present a sensitivity study based on the Loriaux et al. (2016b) setup to investigate the role of large-scale dynamics and environmental conditions with regard to precipitation and the precipitation response to climate change.

For this purpose, we use a large-eddy simulation (LES) model to simulate strong convective precipitation typical for the Netherlands based on composite profiles of the highest 10 percentiles of peak intensities as

described by Loriaux et al. (2016b). Realistic large-scale advective tendencies for heat and moisture are used to drive the simulations. Using these atmospheric conditions as a reference, we systematically vary the relative humidity, stability, and large-scale vertical velocity. Furthermore, this analysis is repeated under a temperature perturbation, to simulate a warmer climate.

Within a convective framework, based on a case study of Loriaux et al. (2016b), we thus aim to

- 1) understand how precipitation depends on atmospheric conditions and lateral forcing, and
- 2) analyze how precipitation is affected by a climate perturbation.

To this end, we first present our methods in section 2. This is followed by the results for the present-day climate in section 3, where we present sensitivity analyses of the moisture budget, attribute changes in the mean precipitation to changes in the precipitation area and changes in the intensity of precipitation, and assess the behavior of extreme precipitation. In section 4, we present an analysis of the response of these precipitation parameters to climate change. Finally, the implications of these results and the conclusions of this study are presented in section 5.

## 2. Methodology and case setup

Loriaux et al. (2016b) provide an event-based analysis that describes the atmospheric conditions accompanying precipitation events grouped by intensity deciles, from 12 h prior to 12 h after the peak intensity of the event. These conditions follow from 20 years of in situ precipitation data over the Netherlands (KNMI 2014), accompanied by a high-resolution model dataset (12 km). This dataset consists of a series of consecutive hindcasts over a period of 20 years using the Regional Atmospheric Climate Model (RACMO; van Meijgaard et al. 2008), forced and initialized by the ERA-Interim reanalysis (Dee et al. 2011).

Using the same datasets as Loriaux et al. (2016b), a strongly precipitating composite case has been derived by grouping together the upper 10% of the precipitation peak intensities from 12 h prior to 12 h after the peak intensity of the event. Only afternoon hours [1200 to 2000 central European time (CET)] have been selected, since we are specifically interested in simulating daytime convective precipitation. The resulting composite case starts at 0500 CET and peaks at 1700 CET. We will use this composite as the standard reference case to be simulated with the Dutch Atmospheric Large Eddy Simulation model (DALES 4.0; Heus et al. 2010; Böing

et al. 2012a), with the ice microphysics scheme described by Böing et al. (2012a).

DALES is an anelastic, high-resolution model that resolves the largest turbulent eddies and parameterizes the smaller turbulent eddies realistically using the well-known turbulent scaling relations in inertial subrange. The prognostic variables are the three wind components  $u$ ,  $v$ ,  $w$ , the liquid water potential temperature  $\theta_l$ , the total water specific humidity  $q_t$ , and finally  $q_r$ , the rain-water specific humidity. In the model, the total water specific humidity and the liquid water potential temperature are defined as

$$q_t = q_v + q_c \quad \text{and} \quad (2)$$

$$\theta_l = \theta - \frac{L_v}{c_{p,d}} \Pi q_c, \quad (3)$$

respectively. Here,  $q_v$  is the specific humidity, and  $q_c$  is the cloud condensate that contains both cloud liquid water and cloud ice. Furthermore,  $\theta$  describes the potential temperature and  $\Pi = (p/p_0)^{R_d/c_{p,d}}$  the Exner function. The latent heat of vaporization is given by  $L_v$ , and the heat capacity for dry air is  $c_{p,d}$ . The gas constant of dry air is  $R_d$ .

All runs are performed over a domain of  $96 \text{ km} \times 96 \text{ km} \times 22 \text{ km}$  with a horizontal resolution of 200 m, and 240 nonequidistant vertical levels, spaced apart 40 m near the surface, up to 175 m at 22 km. This horizontal resolution is supported by Stein et al. (2015). A test run with a larger domain did not have any noticeable effects on the simulation. This was not pursued further in this study. Initial profiles of liquid water potential temperature and total water specific humidity 12 h prior to the peak intensity of the composite case study are used as initial conditions for the reference case (Figs. 1a,b). The resulting relative humidity profile is shown in Fig. 1c. The initial horizontal wind is taken unidirectionally and increases with height from approximately  $6 \text{ m s}^{-1}$  at the surface to  $20 \text{ m s}^{-1}$  at the tropopause (not shown).

Besides initial conditions it is crucial to prescribe realistic large-scale forcings originating from scales larger than the domain of the model. The large-scale forcing terms can be introduced by considering the prognostic equations of  $\phi = \{\theta_l, q_t, u, v, w\}$  averaged over the domain of the LES model in a schematic way:

$$\frac{\partial \bar{\phi}}{\partial t} = \left( \frac{\partial \bar{\phi}}{\partial t} \right)_{\text{LES}} + \left( \frac{\partial \bar{\phi}}{\partial t} \right)_{\text{LS}}, \quad (4)$$

where the overbar denotes an average over the LES domain. The first term on the right-hand side denotes the tendencies resolved by the LES model while the second term hosts contributions from the large scale that

cannot be represented by the LES model. For the heat and moisture equation (i.e.,  $\phi = \{\theta_l, q_t\}$ ) these are essentially the large-scale advection terms. The large-scale advection terms have been derived from the composite event. Comparison of the magnitudes of the advection terms shows that, especially around the maximum peak intensity, the vertical advection term dominates over the horizontal advection term. We therefore approximate the large-scale forcing by only taking the vertical advection term into account; that is,

$$\left( \frac{\partial \bar{\phi}}{\partial t} \right)_{\text{LS}} = -\bar{u} \frac{\partial \bar{\phi}}{\partial x} - \bar{v} \frac{\partial \bar{\phi}}{\partial y} - \bar{w} \frac{\partial \bar{\phi}}{\partial z} \simeq -\bar{w} \frac{\partial \bar{\phi}}{\partial z}. \quad (5)$$

Therefore, the large-scale forcing of heat and moisture in this study can, to first order, simply be prescribed by the large-scale vertical velocity  $\bar{w}$ .

Since the moisture budget plays a crucial role in this study, we derive the resulting vertical integrated moisture budget. The LES resolved tendency for  $\phi = q_t$  is given by

$$\left( \frac{\partial \bar{q}_t}{\partial t} \right)_{\text{LES}} = -\frac{1}{\bar{\rho}} \frac{\partial \bar{\rho} \bar{w}' q_t'}{\partial z} - G, \quad (6)$$

where the first term describes the moistening due to vertical turbulent transport,  $\rho$  denotes the density that only depends on the height, and  $G$  represents the autoconversion rate from  $q_t$  to rain. Primes denote deviations from the domain average values. Substituting (6) and (5) into (4) and vertically integrating gives

$$\int_0^{\text{toa}} \frac{\partial \bar{q}_t}{\partial t} \bar{\rho} dz = - \int_0^{\text{toa}} \bar{\rho} \bar{w} \frac{\partial \bar{q}_t}{\partial z} dz + \bar{\rho}_0 \bar{w}' q_t' - \bar{P}, \quad (7)$$

which describes the moisture budget of the domain. Here  $\bar{P}$  denotes the domain-averaged surface precipitation while the second term on the right-hand side represents the surface evaporation. The vertical advection in (7) represents the large-scale moisture convergence.

The prescribed large-scale vertical velocity  $\bar{w}$  is shown in Fig. 1d and is derived from the composite event that we are aiming to simulate. It increases up to  $t = 12 \text{ h}$ , with a maximum of approximately  $2.4 \text{ cm s}^{-1}$  at 6 km, steadily decreasing until the end of the simulation after that. As a result, the moisture convergence also increases up to 12 h, peaking at approximately  $12.5 \text{ mm day}^{-1}$ , after which it decreases again. In addition, the simulation is forced over time by prescribed values of the surface sensible and latent heat fluxes (Fig. 1e), and the geostrophic wind from 12 h before to 12 h after the peak intensity. These parameters are also taken from the composite case. Since the domain-averaged radiative tendencies are weaker than the

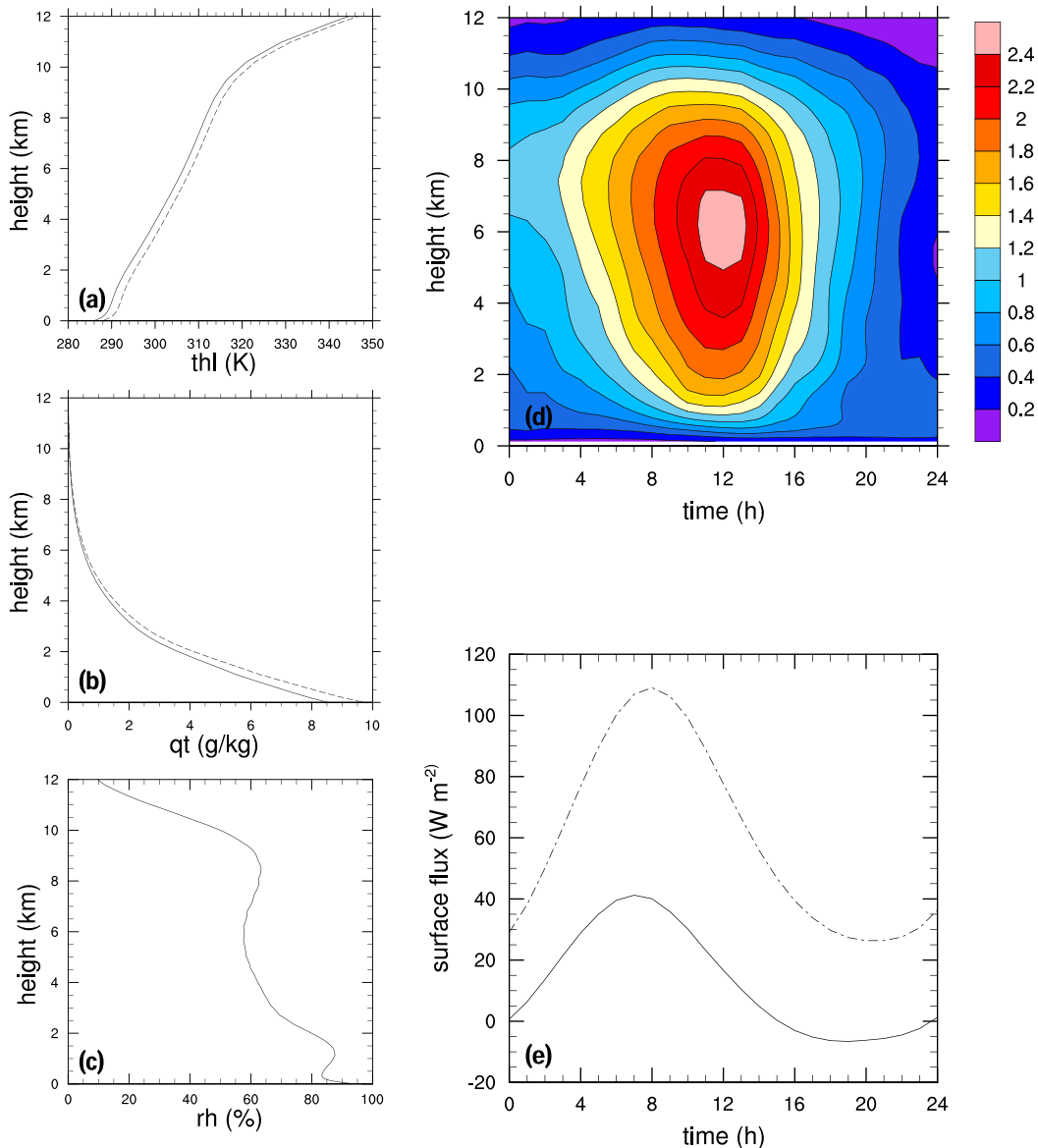


FIG. 1. Model input parameters. The initial reference profiles of (a) liquid water potential temperature, (b) total water humidity, and (c) relative humidity with respect to water. The dashed lines indicate the perturbed climate profiles. Note that for the reference and perturbed climate, the relative humidity profiles are identical. (d) The time–height representation of the large-scale vertical velocity ( $\text{cm s}^{-1}$ ). (e) The sensible (solid) and latent (dashed) heat fluxes at the surface.

heating terms due to convection and large-scale advection (up to  $6 \text{ K day}^{-1}$ ), we have ignored radiative cooling effects in this case for simplicity. All further details of the profiles and forcings used to set up this LES study can be found online at [Loriaux et al. \(2016a\)](#).

In addition to the reference experiment described above, a number of additional experiments are defined in which the relative humidity and vertical stability of the mean initial profiles are systematically varied, as well as the strength of the prescribed large-scale

vertical velocity. This way, the strength of the precipitation response as a function of the initial conditions and the large-scale forcing can be systematically assessed.

The stability is perturbed by subtracting a moist adiabatic correction term from the initial potential temperature profile:

$$\theta = \theta_0 - \alpha \frac{L_v}{c_p \Pi} q_{l,ma}. \quad (8)$$

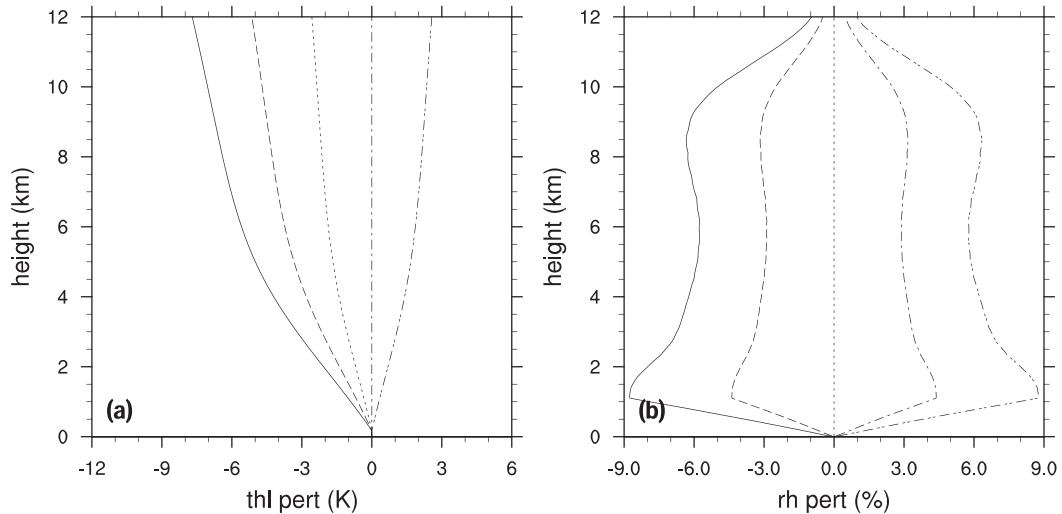


FIG. 2. Perturbations to the initial reference profiles of the (a) liquid water potential temperature and (b) relative humidity.

Here,  $\theta_0$  is the initial profile of the reference experience,  $q_{l,ma}$  is the liquid water humidity for a moist adiabat based on the surface conditions, and  $\alpha$  is the stability factor. For  $\alpha = 0$ , the profile is unchanged and remains close to the moist adiabat. For  $\alpha = 1$ , the profile approaches the dry adiabat, becoming extremely unstable. We have chosen values of  $\alpha$  between  $-0.075$  and  $0.225$  in steps of  $0.075$ , which for the reference experiment leads to potential temperature lapse rates ranging from  $2.1$  to  $3.6 \text{ K km}^{-1}$  at  $1100 \text{ m}$ , a typical level for cloud base in this experiment. Figure 2a shows the perturbations to the reference liquid water potential temperature profile.

The relative humidity (RH) is perturbed by multiplying the initial relative humidity by a factor ranging from  $0.9$  to  $1.1$  in steps of  $0.05$ , from  $1100 \text{ m}$  up. Below that the factor decreases linearly to  $1$  at the surface. The resulting perturbations to the initial RH profile, as well as the profiles themselves are shown in Fig. 2b. This leads to a combined set of  $25$  experiments, based on five stability and five RH perturbations.

To analyze the influence of the large-scale moisture convergence, we have furthermore performed a few additional perturbations to the reference experiment, by multiplying the vertical velocity profiles by a factor of  $0.5$ ,  $2$ , and  $4$ . These perturbations lead to a moisture convergence that peaks at  $6$  to  $60 \text{ mm day}^{-1}$ , ranging from the weakest to strongest perturbation.

Finally, to assess the change in precipitation in a changing climate, we have performed a simple climate change simulation, by uniformly warming the reference experiment by  $2$  degrees, while keeping the relative humidity constant (Sherwood et al. 2010; Dal Gesso et al. 2014). Uniform warming is a reasonable assumption for

midlatitudes, as was previously shown by Attema et al. (2014). Note that, because of our choice of uniform warming, the atmospheric stability with respect to moist processes decreases from present-day to future climate.

In this study, we will focus on the reference experiments of the present-day and future climate in more detail. Since single experiments contain a fair amount of noise due to the chaotic behavior of clouds, we have analyzed an ensemble of five members for both reference experiments in order to give an idea of the uncertainty of the results. In DALES, simulations are initialized by randomly perturbing the initial  $\theta_t$  and  $q_t$  profiles. The array of random numbers used for these perturbations is determined by the randomization seed. Each ensemble member has a different randomization seed, but the same input profiles. These ensembles are used when analyzing the reference state of the present and future climate.

### 3. Present-day climate

The moisture budget plays a key role in understanding how precipitation responds to different forcings and atmospheric conditions. A symbolic representation of the vertically integrated moisture budget (7) is

$$S = M + E - P. \quad (9)$$

Moisture is added to the domain through lateral moisture convergence  $M$  and the surface evaporation  $E$ , and lost through precipitation  $P$ . Any imbalance between the inflow and precipitation will affect the moisture content of the domain. The difference between the gain

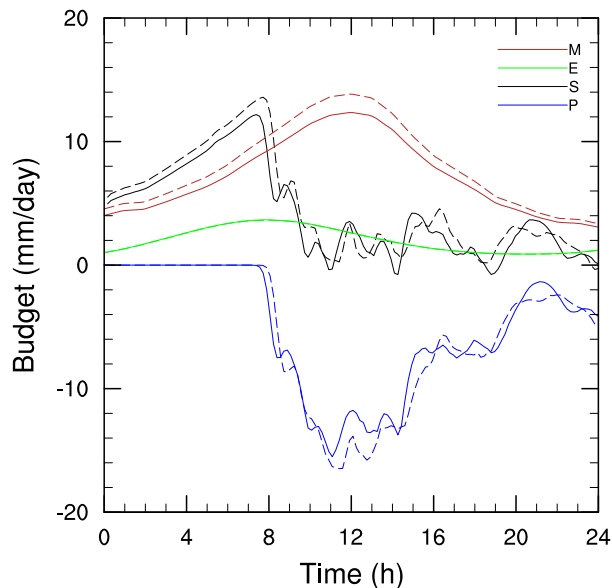


FIG. 3. Moisture budget of the five-member ensemble mean reference experiment for the current (solid) and warm (dashed) climate.

and loss term makes up the moisture tendency, which describes if the domain is becoming moister or drier. This is the storage term  $S$ . If more moisture is added to the system but the storage term remains relatively the same or decreases, the precipitation efficiency increases, and vice versa.

First, we take a look at the temporal development of the moisture budget of the reference experiment. To this end, the temporal evolution of the moisture budget is shown in Fig. 3. The moisture input due to the latent heat flux at the surface maximizes at  $t = 8$  h, at  $3.5 \text{ mm day}^{-1}$ . The lateral moisture convergence dominates the moisture input, peaking at  $t = 12$  h, at  $12.5 \text{ mm day}^{-1}$ . In response to the increasing moisture input, the total water specific humidity of the domain increases, as can be seen in the storage term, until it starts to rain at  $t = 8$  h. The precipitation very quickly picks up, causing the moisture tendency to drop. Following the moisture convergence, most precipitation falls between  $t = 10$  h and  $t = 15$  h, peaking at approximately  $-15 \text{ mm day}^{-1}$ .

Figure 4 shows a precipitation snapshot of the domain at  $t = 12$  h, at which time it has been raining for a while, and the precipitation intensities are high. There are several small precipitation clusters, with diameters of approximately 5 km, most of which have maximum precipitation intensities that exceed  $5 \text{ mm (10 min)}^{-1}$ . The largest cluster is located at  $x = 30 \text{ km}$ ,  $y = 50 \text{ km}$ , and spans approximately 10 km by 20 km. In this cluster, precipitation intensities are found that are far higher

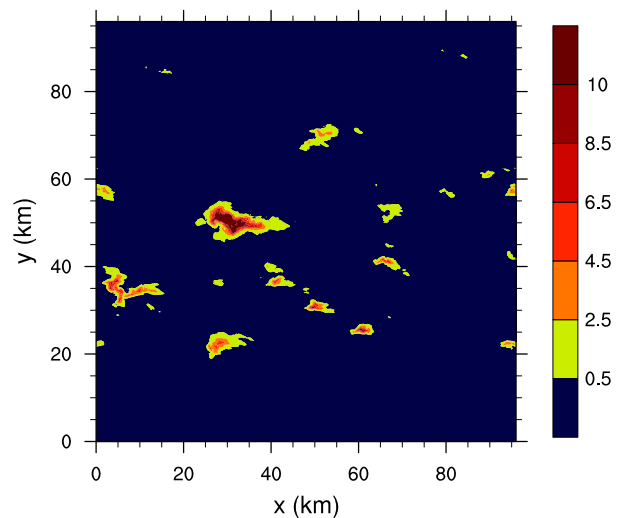


FIG. 4. Precipitation intensity ( $\text{mm}/10 \text{ min}$ ) snapshot at the surface, at  $t = 12$  h.

than  $10 \text{ mm}/10 \text{ min}$ . There are no clear signs of large-scale organization.

As can be seen in Fig. 3, the amount of precipitation weakens as the moisture convergence starts to decrease during the second half of the experiment. Once the precipitation sets in at  $t = 8$  h, the moisture inflow is closely, but never completely, balanced by precipitation, which means that the moisture content of the domain continues to slowly increase over time.

Next, we analyze the time-averaged moisture budget of the domain:

$$\langle \text{IN} \rangle - \langle P \rangle = \langle S \rangle, \quad (10)$$

where  $\langle \dots \rangle = \int_{0\text{h}}^{24\text{h}} \dots dt / t_{\text{total}}$ , and  $\text{IN} = M + E$ . The sensitivity of the time-integrated moisture budget to initial relative humidity and stability is shown in the left column of Fig. 5. The relative humidity perturbations are shown along the  $x$  axis and the stability perturbations along the  $y$  axis, with the most unstable, moist (stable, dry) conditions at the top right (bottom left). Figure 5a shows the sensitivity of the moisture input in the present-day climate. As the latent heat flux is fixed, the dependence of the moisture input on the initial relative humidity and stability is completely due to the moisture convergence, and maximizes for more stable, wet conditions. The moisture inflow increases by approximately 9% from the lowest to highest values.

The moisture loss term consists of the mean precipitation rate (Fig. 5b). It is influenced by both stability and relative humidity. With the highest values corresponding to the more unstable experiments with high relative humidity, this result is consistent with the results found by Böing et al. (2012b). The mean precipitation

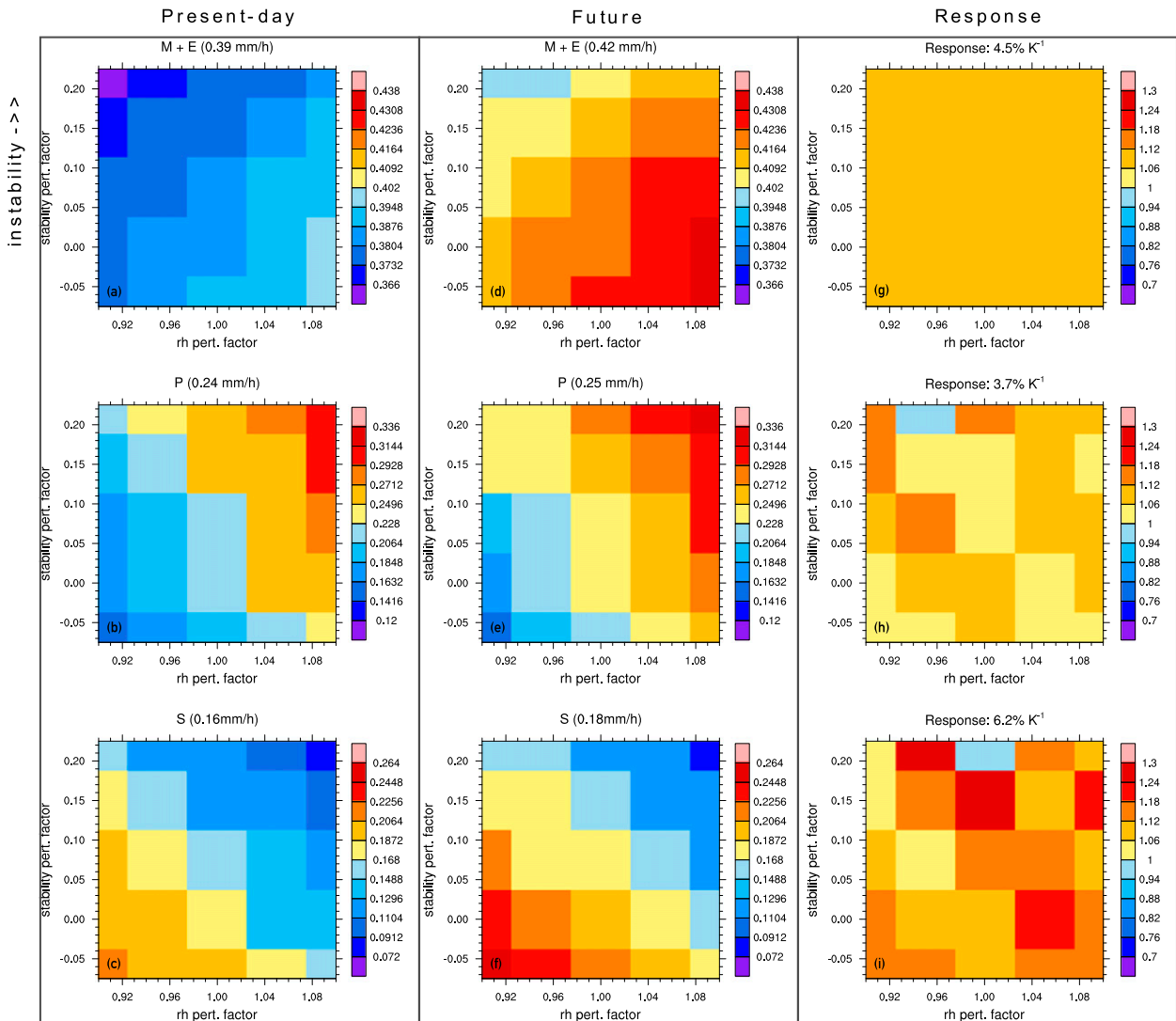


FIG. 5. Phase space results of the moisture budget, showing the (top) moisture input, (middle) precipitation, and (bottom) storage for the (a)–(c) present-day and (d)–(f) future climate, and (g)–(i) climate response. Relative humidity perturbations are shown along the x axis; stability perturbations along the y axis.

rate approximately doubles from dry, stable to moist, unstable conditions.

Since the sensitivity of the moisture convergence to RH and stability conditions is far lower than the domain averaged precipitation, the storage term approximately mirrors the precipitation (Fig. 5c). Storage is lowest for moist, unstable conditions, and highest for dry, stable conditions, where the mean precipitation is lowest. Similar to the precipitation, we see approximately doubling of the storage term over the phase space.

The domain-averaged precipitation is not very informative concerning the actual precipitation intensity as the area of precipitation is less than 10% (see Fig. 4). We will therefore reserve the term “precipitation intensity” for the precipitation conditioned on the

precipitating area. To this end, the mean precipitation rate  $\langle \bar{P} \rangle$  can be further decomposed into the mean precipitation intensity,  $\langle I \rangle$ , and the mean precipitation area fraction,  $\langle a \rangle$ , the fraction of grid columns with precipitation reaching the surface:

$$\langle \bar{P} \rangle = \langle a \rangle \langle I \rangle. \tag{11}$$

A precipitation threshold of  $0.01 \text{ mm (10 min)}^{-1}$  is used.

Figure 6 shows the decomposition of the mean precipitation into the precipitation area fraction (Fig. 6a), and the mean intensity (Fig. 6b). The area fraction shows that, on average, 5.5% of the domain is covered by precipitation. It is mostly determined by the relative humidity, and nearly doubles from the dry to moist

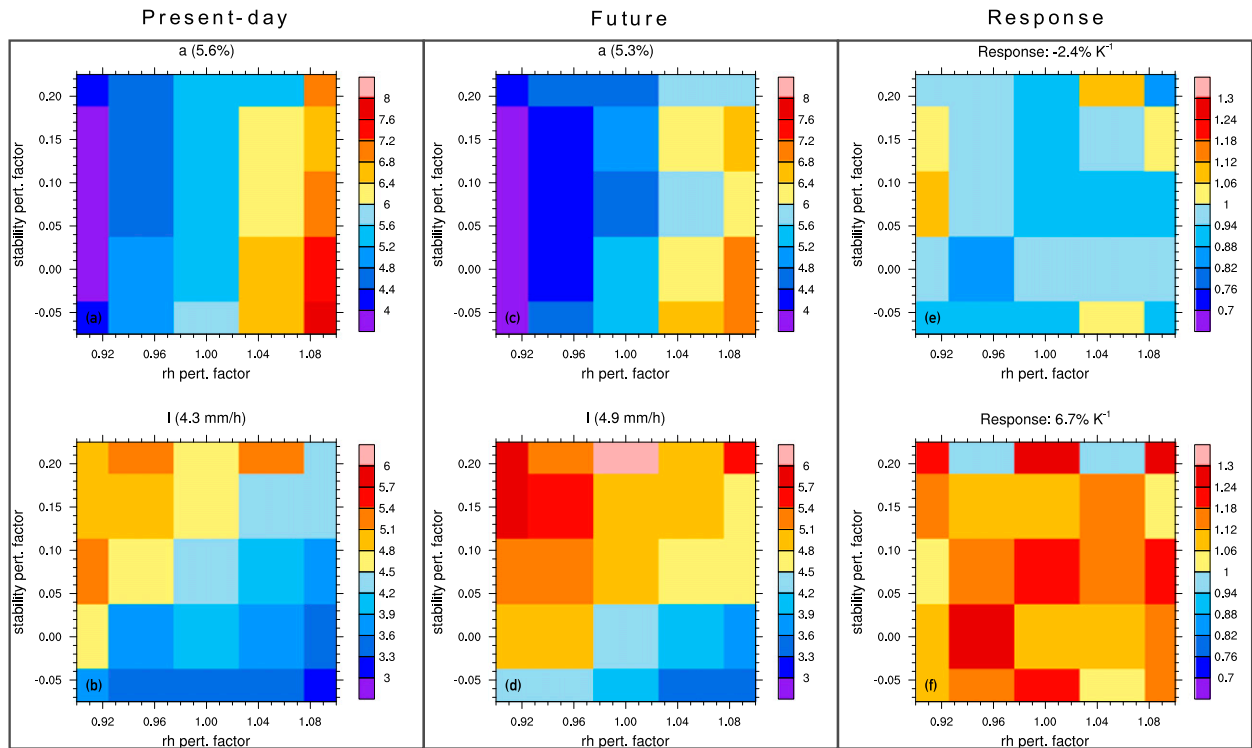


FIG. 6. Phase space results of the (top) area fraction and (bottom) precipitation intensity for the (a),(b) present-day and (c),(d) future climate, and (e),(f) climate response. Relative humidity perturbations are shown along the x axis; stability perturbations along the y axis.

perturbations. While the change in area fraction over the phase space is comparable to the mean precipitation, the stability hardly affects the area fraction.

Consequently, the mean intensity is not influenced by RH in the same way as the mean precipitation seen in Fig. 5c. Instead, the mean intensity is highest for unstable but drier conditions. A physical interpretation of these results is that when the relative humidity is high, it rains sooner, leading to many light events. When the relative humidity is lower, more buildup is necessary before it rains, leading to fewer but stronger events. The increase in precipitation intensity with instability follows from increased updraft velocities (not shown). Averaging at  $4.3 \text{ mm h}^{-1}$ , the mean intensity increases by approximately 60% over the range of perturbations.

So far, we have focused on the mean precipitation. Although the mean state already represents strong convective precipitation by means of the experimental setup, we will also focus on the extremes of this experiment. Figure 7a shows the probability of exceedance distribution of the precipitation intensity (data exceeding the precipitation threshold) for the five-member ensemble mean reference experiment of the present-day climate (solid line). The gray band denotes  $\pm 1$  standard deviation to the mean. Only approximately 20% of the precipitation intensities exceed  $1 \text{ mm (10 min)}^{-1}$ ; however,

the highest intensities go beyond  $25 \text{ mm (10 min)}^{-1}$ . As can be expected, the standard deviation increases with decreasing probability of exceedance. Since we want to ensure that the sensitivity to the different perturbations can be reliably estimated, we will use the 99th percentile of the precipitation intensity (1% exceedance) when looking at precipitation extremes. This corresponds to  $\sim 6.5 \text{ mm (10 min)}^{-1}$  for the reference experiment. The equivalent percentile for precipitation is approximately the 99.95th percentile (0.05% exceedance).

Figure 8a shows the phase space for the extreme precipitation intensity. Similar to the mean intensity, the extreme precipitation is sensitive to stability and RH. When it is raining, a relatively dry but unstable atmosphere will lead to the strongest precipitation intensities. This supports the theory that there is more precipitation build-up for dry but unstable conditions, eventually leading to stronger intensities. With an average extreme intensity of  $43.6 \text{ mm h}^{-1}$ , the extreme intensity increases by 60% across the phase space.

However, extreme precipitation (not conditioned on the precipitation area) no longer depends on the initial RH, and increases as the initial stability of the atmosphere decreases (Fig. 8b). While the mean and extreme intensities share the same preference for drier, unstable conditions, extreme precipitation is not predisposed

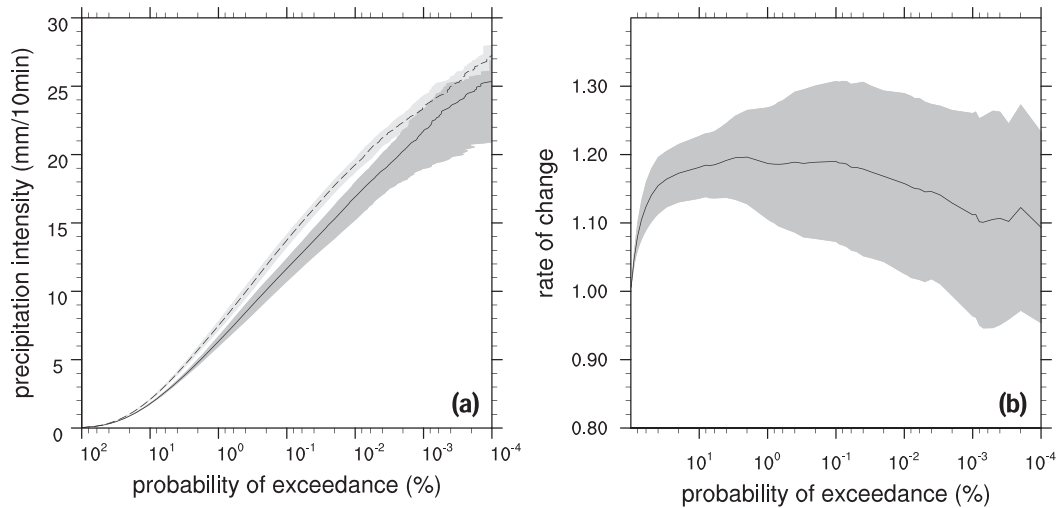


FIG. 7. (a) Probability of exceedance for the present-day (solid) and perturbed climate (dashed) and (b) percentile response to the climate perturbation, using a precipitation intensity threshold of  $0.01 \text{ mm} (10 \text{ min})^{-1}$ .

toward high initial RH conditions like mean precipitation is. This is because the increase of the mean precipitation rate with increasing RH is caused by an increase in the area fraction, but a decrease in intensity. As a result, the upper percentiles of the distribution of the precipitation rate are not strongly affected by the RH for the range investigated in this study. Note that for low values of relative humidity a dependence of the extreme precipitation intensity is expected as the lack of moisture availability begins to play a role.

We next examine the role of large-scale dynamics on precipitation by performing a few coarse perturbations to the large-scale vertical velocity, and hence the moisture convergence. Figure 9a shows the relative change of the different components of the moisture budget due to these perturbations, with respect to the reference experiment. As a result of these perturbations, the total moisture input increases slightly less than the  $w$  perturbation factor. This, of course, is due to the unchanging surface LHF, which makes up for part of the moisture input. Indeed, mean precipitation increases by more than the perturbation factor—up to 5.2 times the mean precipitation of the reference experiment.

To assess whether this change in mean precipitation is achieved by an increase in the area fraction or intensity, we again decompose the mean precipitation rate. The precipitation intensity ( $I$ ) and area fraction ( $a$ ) are also shown in Fig. 9a. It is clear that the increase in mean intensity is caused by an increase in the precipitation area fraction, with a slight decrease in the mean intensity for larger moisture convergence. In other words, because of an increase in the large-scale vertical velocity, it rains more, rather than more intensely.

It is possible that this increase in the area fraction can simply be explained by the fact that in a domain that is favorable to convection, more large-scale uplift triggers more convective updrafts by lifting parcels to a level where they become unstable. In this setup, while the area fraction increases, the individual precipitation cells do not appear to grow much larger for higher moisture convergence. The area fraction is thus mostly increased because more of these cells are present in the domain, rather than a higher level of organization. This should be further investigated in future work.

The same relations are seen for extreme precipitation ( $P_{\text{extr}}$ ), although they are more subtle. While the extreme precipitation shows a small increase with increasing moisture convergence, the extreme intensity ( $I_{\text{extr}}$ ) shows the same weak decrease as the mean intensity. Since the extreme precipitation increases with increasing moisture convergence, the decrease in the extreme intensity is probably caused by a shift in the intensity distribution toward weaker events, even though stronger intensities do also occur. However, it is clear that the moisture convergence has a stronger effect on the area fraction than the precipitation intensity.

This concludes our sensitivity analysis of the present-day climate. The different effects of the stability and moisture convergence perturbations, both leading to an increase in precipitation, are visualized in Fig. 10. While increasing the atmospheric instability leads to more intense precipitation without greatly affecting the area fraction, moisture convergence leads to a larger precipitation area without substantially influencing the intensity. The relative humidity has two opposing effects. First, the higher the relative humidity, the more

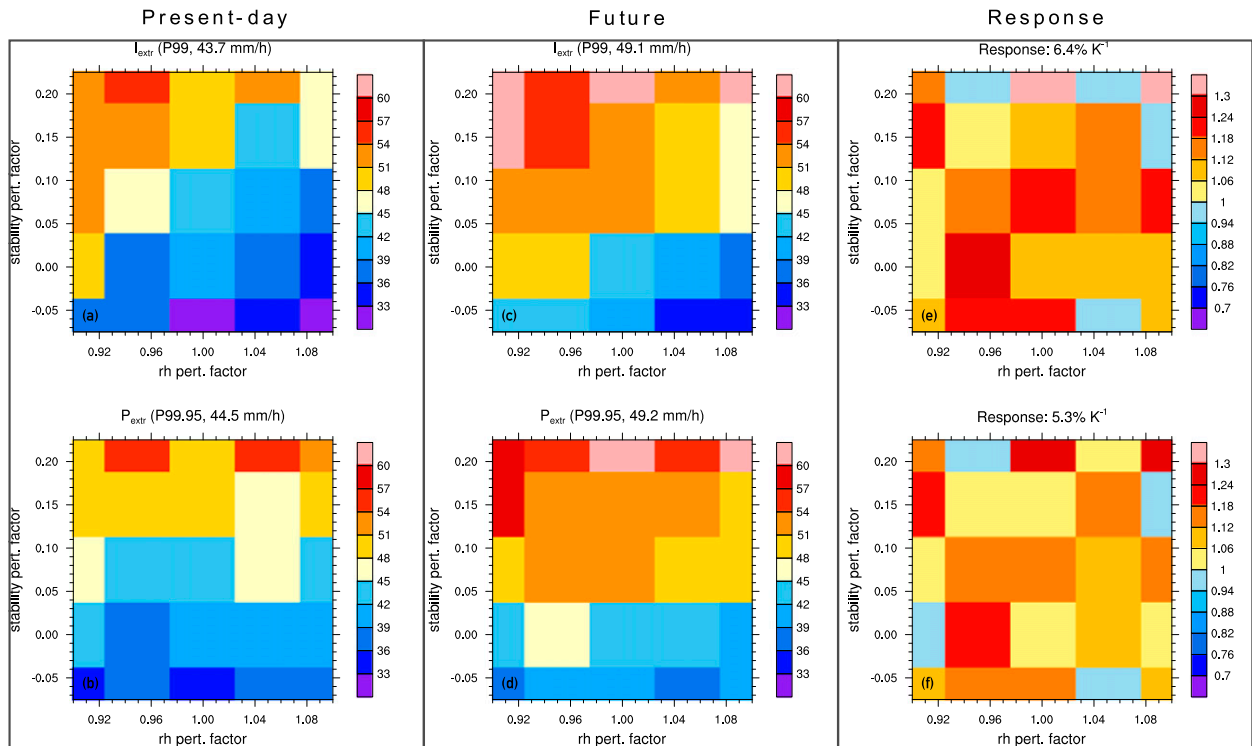


FIG. 8. Phase space results of the (top) extreme intensity and (bottom) extreme precipitation for the (a),(b) present-day and (c),(d) future climate, and (e),(f) climate response. Relative humidity perturbations are shown along the  $x$  axis; stability perturbations along the  $y$  axis.

precipitation; this is best seen in the precipitation area fraction. Second, the lower the relative humidity, the higher the intensity. This is best seen in the sampled phase spaces, after the effect of the area fraction has been removed.

#### 4. Future climate

We have performed a simple warming experiment by perturbing the initial temperature profile by 2 K while keeping the relative humidity constant. For comparison with the present-day climate, the same sensitivity analyses of the relative humidity and stability, and finally the vertical velocity, have been performed for the warm setup.

The dashed lines in Fig. 3 show the moisture budget of the warm run. It is clear that the temporal evolution of the experiment is quite similar to the reference. The moisture convergence rises as a result of the increase in total water specific humidity. In fact, with a growth of  $7\% \text{ K}^{-1}$ , the moisture convergence is almost completely determined by the CC relation. This can be understood when we approximate the specific humidity of the future climate as  $q_+ \approx q_{\text{ref}}(1 + 0.07\Delta T)$  to account for the moisture increase of CC. After substituting this into  $M$ , it can be easily shown that the future climate moisture

convergence equals the present-day moisture convergence multiplied by the CC increase factor. Note that in actuality, the CC factor slightly increases with height in the troposphere.

The center column of Fig. 5 shows the phase spaces of the time integrated moisture budget components for the warm setup. The right column shows the rate of change between the warm and present-day climate, normalized by the temperature perturbation. With an increase of approximately 9% from dry, unstable conditions to moist, stable conditions, the sensitivity of the mean moisture input (Fig. 5d) to initial stability and relative humidity remains the same as the for the present-day climate. As a result, the increase in moisture input from the present-day to future climate is very robust, at  $4.5\% \text{ K}^{-1}$ , with a spread of  $4.2\%$  to  $4.6\% \text{ K}^{-1}$  (Fig. 5g). The response of the moisture input is weaker than the response of the moisture convergence alone because the surface evaporation remains constant.

Similar to the present-day climate, the precipitation rate of the future climate also increases from stable and dry to unstable and wet conditions (Fig. 5e). The mean precipitation increases on average by  $3.7\% \text{ K}^{-1}$  (Fig. 5h). There is no clear sensitivity pattern in the response, which means that the change in mean precipitation is not very sensitive to the initial conditions.

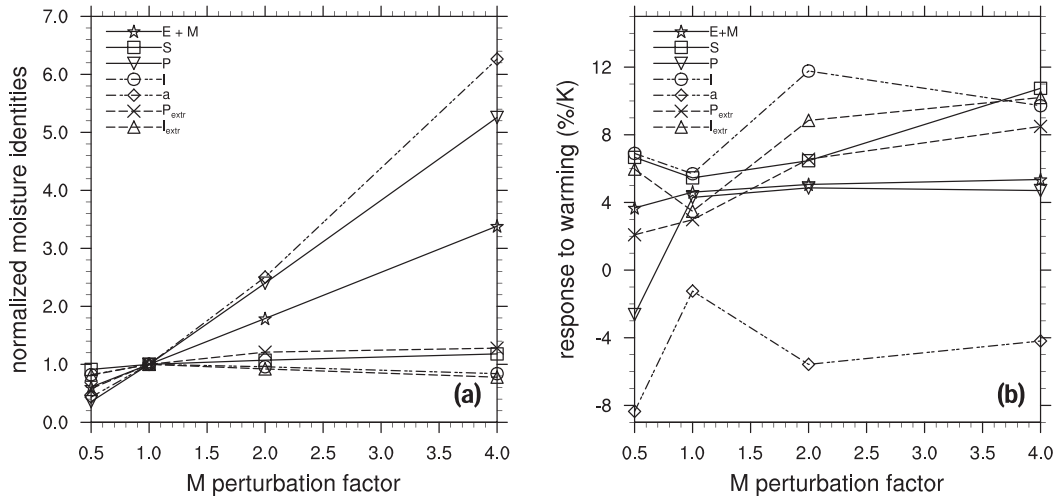


FIG. 9. (left) Response of the different components of the moisture budget and decomposition of  $P$  into the area fraction and precipitation intensity to vertical velocity perturbations in the present-day climate. Results are normalized for the reference (perturbation factor = 1). (right) The response of mean and extreme precipitation, intensity, and the area fraction to climate change for perturbations of the vertical velocity.

The storage term (Fig. 5f) again depends on stability and RH the same way as in the present-day climate, increasing from moist, unstable conditions to drier, more stable conditions. From present-day to future climate, the storage term grows by approximately  $6.2\% \text{ K}^{-1}$  (Fig. 5i). The variation in this phase space is quite high, but again no dependence on stability or relative humidity can be observed.

To determine whether the relative importance of the area fraction and mean wet precipitation intensity changes due to the climate perturbation, we return now to Fig. 6. A quick comparison of the area fraction (Fig. 6c) and mean precipitation intensity (Fig. 6d) with the reference shows that the dependencies of the moisture budget on initial stability and relative humidity do not change due to warming. Furthermore, as can be seen in Figs. 6e and 6f, respectively, the response does not depend on the initial relative humidity or stability for either component. The area fraction shows a slight decrease, of approximately  $2.4\% \text{ K}^{-1}$  due to warming, whereas the mean intensity increases by approximately

$6.7\% \text{ K}^{-1}$ . This means that as a result of warming it will on average rain slightly less, but more intensely.

The probability of exceedance for the five-member ensemble run of the warm climate reference experiment (Fig. 7a, dashed) shows that precipitation intensities are consistently higher than in the present-day climate. Figure 7b shows the fractional rate of change of percentiles of the precipitation intensity for the ensemble reference experiments of the present-day and future climate. From the 60th to the 99.99th percentile, the fractional rate of change shows a fairly robust increase, between  $7\%$  and  $10\% \text{ K}^{-1}$ . For higher percentiles the fractional rate of change is slightly lower, with an increase of  $5\%$ – $7\% \text{ K}^{-1}$ . The gray band denotes  $\pm 1$  standard deviation, showing that the spread is quite large, especially for the high percentiles.

Figure 8 shows the dependence of extreme precipitation on initial relative humidity and stability in the warm climate (Figs. 8c,d) and the rate of change from present-day to warm climate (Figs. 8e,f). The climate perturbation does not change the dependencies of the

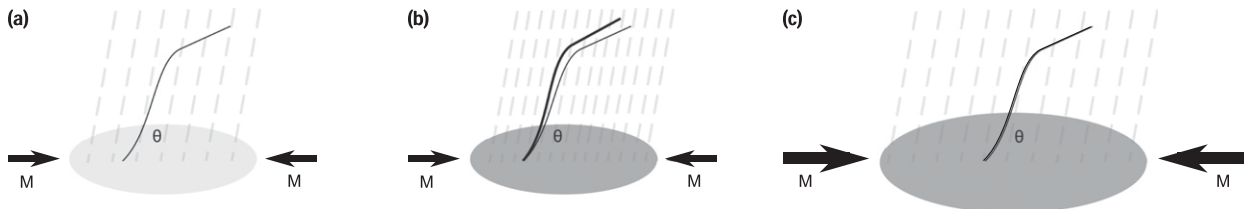


FIG. 10. Conceptual drawing showing the effects of (b) stability and (c) moisture convergence perturbations on precipitation, with respect to (a) the reference experiment. Destabilization and increased moisture convergence both lead to an increase in precipitation. This occurs through intensification in (b) and an increase in the precipitation area fraction in (c), respectively.

extremes within the phase spaces, but it does lead to an increase in both extreme precipitation and intensity. On average, the extreme intensity increases by  $6.4\% \text{ K}^{-1}$  due to the climate perturbation (Fig. 8e), which is slightly below the rise in the mean intensity. Because of the decrease in the area fraction, the response of extreme precipitation to the climate perturbation is a bit weaker ( $5.3\% \text{ K}^{-1}$ ; Fig. 8f).

The climate response of the moisture budget, precipitation components, and extremes for perturbations of the large-scale dynamics through  $M$  are shown in Fig. 9b. The response of the components of the moisture budget show that with an increase of approximately  $4.5$  to  $5\% \text{ K}^{-1}$ , the response of the moisture gain ( $M + E$ ) and loss ( $P$ ) terms are hardly affected by enhancing the large-scale dynamics. This leads to an increase of the storage response  $S$  from approximately  $5.5\% \text{ K}^{-1}$  up to  $11\% \text{ K}^{-1}$  with increasing perturbations of  $M$ . For weaker large-scale dynamics (a perturbation factor of 0.5), the mean precipitation decreases as a result of warming, and the storage again has a strong, positive response. Overall, the budget components do not show clear systematic dependencies of the moisture convergence.

Similar to Fig. 6e, the area fraction decreases due to warming. With a response between  $-8\%$  and  $-1\% \text{ K}^{-1}$ , there is quite a large spread, but no clear dependence of the response on the amount of large-scale forcing applied. The responses of the mean ( $I$ ) and extreme ( $I_{\text{extr}}$ ) intensity also have a large spread, in the range of  $6\%$  to  $12\% \text{ K}^{-1}$  and  $4\%$  to  $10\% \text{ K}^{-1}$ , respectively, without a clear dependency on the large-scale dynamics. The response of the extreme precipitation does appear to increase with increasing moisture convergence. As was found in the sensitivity analysis with respect to relative humidity and stability, the response of the extreme intensity is stronger than the extreme precipitation response.

Overall, these results suggest that the changes in precipitation characteristics in a future climate are not very sensitive to the relative humidity, stability, and moisture convergence. As a result of warming, more moisture is brought to the system, leading to moistening (storage), and higher mean and extreme precipitation. This is accomplished by means of higher precipitation intensities, while the precipitation area fraction slightly decreases.

## 5. Discussion and conclusions

We have set up a composite LES case for convective precipitation using strong large-scale forcing based on idealized profiles for the highest 10 percentiles of peak

intensities over the Netherlands, as described by Loriaux et al. (2016b). In this setting, we have performed sensitivity analyses for atmospheric stability, large-scale moisture convergence, and relative humidity and have compared present-day climate to a warmer future climate.

Sensitivity analysis has shown that precipitation responds differently to changes in relative humidity, stability, and large-scale moisture convergence. Mean precipitation increases with relative humidity. However, decomposition in intensity and precipitation area fraction shows that while the area fraction also increases with relative humidity, the intensity decreases. This indicates that when the relative humidity rises it rains sooner, leading to more but weaker precipitation due to the lack in buildup of precipitable water prior to the event.

By enhancing the instability of the atmosphere or the moisture convergence, the mean precipitation increases. However, this increase is caused by two different effects. While the rise in precipitation with heightened instability is caused by an increase in the mean intensity with only minor changes in the area fraction, the opposite is true for the increased precipitation rate due to large-scale moisture convergence. Here, the increase in the mean precipitation rate is caused by a very distinct expansion of the area fraction, but the mean intensity remains relatively constant.

Changes in the behavior of extreme versus mean precipitation with respect to the relative humidity and large-scale moisture convergence indicate a shift in the precipitation distribution. For example, because of an increase in relative humidity, nonprecipitating points become weakly precipitating points. This does not influence the extreme precipitation rate, but does lead to a shift in the intensity distribution toward weaker intensities. As a result, the extreme intensity decreases with increasing relative humidity, while extreme precipitation remains constant with respect to relative humidity perturbations.

Similar to the precipitation response to relative humidity, the rise in mean precipitation with increasing moisture convergence is caused by an expansion of the area fraction. Therefore, it is not surprising that the extreme intensity decreases with increasing moisture convergence. However, unlike the relative humidity, the moisture convergence does lead to a small increase in the extreme precipitation rate. This indicates that while the intensity distribution does shift toward lighter intensities, higher intensities also increase.

The sensitivities of mean and extreme precipitation to the initial relative humidity, stability, and large-scale forcing in the future climate are very similar to the

present-day climate. As a result, no patterns can be found in the phase spaces of the precipitation response, indicating that the relations between precipitation and large-scale conditions in the present-day climate are robust for a changing climate.

The precipitation response to climate change is weaker than expected based on observed relations between temperature and precipitation intensity in the present-day climate. The response of the precipitation intensity follows CC scaling (6%–7% K<sup>-1</sup>) for both mean and extreme intensities. The area fraction decreases from present-day to future climate, causing the precipitation response to be lower than the response of the precipitation intensity. In other words, our climate perturbation indicates that with warming it will rain more intensely but in fewer places, leading to a mean increase in precipitation of 3.5% K<sup>-1</sup>.

This setup has provided useful insights regarding the sensitivity of precipitation to large-scale forcing and atmospheric conditions, and the continuity of the phase space patterns gives us confidence in the results. However, it might be useful to study in more detail why this setup did not reach expected super-CC precipitation responses. We have seen in Eq. (1) that for local precipitation a response below CC scaling can be caused by dynamics or the precipitation efficiency. Here, the dynamical contribution is connected to the updraft velocity, while the precipitation efficiency contains information on the entrainment and detrainment, autoconversion rate, and other processes controlling the precipitation intensity. Using conditionally sampled profiles, it is possible to approximate a convective plume. This can be used to determine the climate response for a constant precipitation efficiency based on Eq. (1) to examine if the combined dynamic and thermodynamic contributions explain the precipitation intensity response found in this study of 6.5% K<sup>-1</sup>:

$$I_{\text{th},d} = - \int_{z_b}^{z_t} w_c \frac{\partial q_{s,c}}{\partial z} \rho dz, \quad (12)$$

where the subscript *c* indicates that it concerns fields that are averaged only over the active convective updrafts. A positive dynamical contribution will cause the approximated intensity response to exceed CC scaling, and vice versa. Strong deviations of the response of  $I_{\text{th},d}$  from 6.5% K<sup>-1</sup> would suggest that the precipitation efficiency is an important factor in determining the precipitation response. Preliminary results using cloud core sampled profiles ( $q_l > 0$  and  $\theta_v > 0$ ) do suggest a strong dynamical component, leading to a super-CC response of  $I_{\text{th},d}$ . Future work should focus on following precipitation events by means of a clustering scheme, in order to

better connect the large-scale conditions to the event-scale (thermo)dynamics and efficiency.

*Acknowledgments.* The authors thank Steef Böing and Huug Ouwersloot for their useful comments regarding the use of DALES. This study was funded by Knowledge for Climate, theme 6. Furthermore, NWO/Surfsara sponsored the use of supercomputer facilities. Geert Lenderink acknowledges financial support from the EU Grant INTENSE (FP7-IDEAS-ERC, Project 617329).

## REFERENCES

- Allen, M. R., and W. J. Ingram, 2002: Constraints on future changes in climate and the hydrological cycle. *Nature*, **419**, 224–232, doi:10.1038/nature01092.
- Attema, J. J., J. M. Loriaux, and G. Lenderink, 2014: Extreme precipitation response to climate perturbations in an atmospheric mesoscale model. *Environ. Res. Lett.*, **9**, 014003, doi:10.1088/1748-9326/9/1/014003.
- Berg, P., C. Moseley, and J. O. Haerter, 2013: Strong increase in convective precipitation in response to higher temperatures. *Nat. Geosci.*, **6**, 181–185, doi:10.1038/ngeo1731.
- Blenkinsop, S., S. C. Chan, E. J. Kendon, N. M. Roberts, and H. J. Fowler, 2015: Temperature influences on intense UK hourly precipitation and dependency on large-scale circulation. *Environ. Res. Lett.*, **10**, 054021, doi:10.1088/1748-9326/10/5/054021.
- Böing, S. J., H. J. J. Jonker, A. P. Siebesma, and W. W. Grabowski, 2012a: Influence of the subcloud layer on the development of a deep convective ensemble. *J. Atmos. Sci.*, **69**, 2682–2698, doi:10.1175/JAS-D-11-0317.1.
- , A. P. Siebesma, J. D. Korpershoek, and H. J. J. Jonker, 2012b: Detrainment in deep convection. *Geophys. Res. Lett.*, **39**, L20816, doi:10.1029/2012GL053735.
- Dal Gesso, S., A. P. Siebesma, S. R. de Roode, and J. M. van Wessem, 2014: A mixed-layer model perspective on stratocumulus steady states in a perturbed climate. *Quart. J. Roy. Meteor. Soc.*, **140**, 2119–2131, doi:10.1002/qj.2282.
- Davies, L., C. Jakob, P. May, V. V. Kumar, and S. Xie, 2013: Relationships between the large-scale atmosphere and the small-scale convective state for Darwin, Australia. *J. Geophys. Res.*, **118**, 11 534–11 545, doi:10.1002/jgrd.50645.
- Dee, D. P., and Coauthors, 2011: The ERA-Interim reanalysis: Configuration and performance of the data assimilation system. *Quart. J. Roy. Meteor. Soc.*, **137**, 553–597, doi:10.1002/qj.828.
- Emori, S., and S. J. Brown, 2005: Dynamic and thermodynamic changes in mean and extreme precipitation under changed climate. *Geophys. Res. Lett.*, **32**, L17706, doi:10.1029/2005GL023272.
- Hardwick-Jones, R., S. Westra, and A. Sharma, 2010: Observed relationships between extreme sub-daily precipitation, surface temperature, and relative humidity. *Geophys. Res. Lett.*, **37**, L22805, doi:10.1029/2010GL045081.
- Heus, T., and Coauthors, 2010: Formulation of and numerical studies with the Dutch Atmospheric Large-Eddy Simulation (DALES). *Geosci. Model Dev.*, **3**, 415–444, doi:10.5194/gmdd-3-99-2010.
- IPCC, 2014: *Climate Change 2013: The Physical Science Basis*. T. F. Stocker et al., Eds., Cambridge University Press, 1535 pp.

- KNMI, 2014: Uurgegevens van het weer in Nederland. Accessed 13 November 2014. [Available online at <https://www.knmi.nl/nederland-nu/klimatologie/uurgegevens>.]
- Lenderink, G., and E. van Meijgaard, 2008: Increase in hourly precipitation extremes beyond expectations from temperature changes. *Nat. Geosci.*, **1**, 511–514, doi:10.1038/ngeo262.
- , and —, 2010: Linking increases in hourly precipitation extremes to atmospheric temperature and moisture changes. *Environ. Res. Lett.*, **5**, 025208, doi:10.1088/1748-9326/5/2/025208.
- , and J. Attema, 2015: A simple scaling approach to produce climate scenarios of local precipitation extremes for the Netherlands. *Environ. Res. Lett.*, **10**, 085001, doi:10.1088/1748-9326/10/8/085001.
- Loriaux, J. M., G. Lenderink, S. R. de Roode, and A. P. Siebesma, 2013: Understanding convective extreme precipitation scaling using observations and an entraining plume model. *J. Atmos. Sci.*, **70**, 3641–3655, doi:10.1175/JAS-D-12-0317.1.
- , —, and A. P. Siebesma, 2016a: Composite case of conditions leading to high peak precipitation intensities in the Netherlands [data files]. [Available online at doi:10.4121/uuid:e066b7f5-f83b-406b-93e8-6ba3eb3659eb.]
- , —, and —, 2016b: Peak precipitation intensity in relation to atmospheric conditions and large-scale forcing at mid-latitudes. *J. Geophys. Res. Atmos.*, **121**, 5471–5487, doi:10.1002/2015JD024274.
- Min, S.-K., X. Zhang, F. W. Zwiers, and G. C. Hegerl, 2011: Human contribution to more-intense precipitation extremes. *Nature*, **470**, 378–381, doi:10.1038/nature09763.
- Mishra, V., J. M. Wallace, and D. P. Lettenmaier, 2012: Relationship between hourly extreme precipitation and local air temperature in the United States. *Geophys. Res. Lett.*, **39**, L16403, doi:10.1029/2012GL052790.
- Muller, C., 2013: Impact of convective organization on the response of tropical precipitation extremes to warming. *J. Climate*, **26**, 5028–5043, doi:10.1175/JCLI-D-12-00655.1.
- , L. E. Back, and P. A. O’Gorman, 2011: Intensification of precipitation extremes with warming in a cloud-resolving model. *J. Climate*, **24**, 2784–2800, doi:10.1175/2011JCLI3876.1.
- O’Gorman, P. A., 2012: Sensitivity of tropical precipitation extremes to climate change. *Nat. Geosci.*, **5**, 697–700, doi:10.1038/ngeo1568.
- , 2015: Precipitation extremes under climate change. *Curr. Climate Change Rep.*, **1**, 49–59, doi:10.1007/s40641-015-0009-3.
- , and T. Schneider, 2009a: The physical basis for increases in precipitation extremes in simulations of 21st-century climate change. *Proc. Natl. Acad. Sci. USA*, **106**, 14773–14777, doi:10.1073/pnas.0907610106.
- , and —, 2009b: Scaling of precipitation extremes over a wide range of climates simulated with an idealized GCM. *J. Climate*, **22**, 5676–5685, doi:10.1175/2009JCLI2701.1.
- Pall, P., T. Aina, D. A. Stone, P. A. Stott, T. Nozawa, A. G. J. Hilberts, D. Lohmann, and M. R. Allen, 2011: Anthropogenic greenhouse gas contribution to flood risk in England and Wales in autumn 2000. *Nature*, **470**, 382–385, doi:10.1038/nature09762.
- Romps, D. M., 2011: Response of tropical precipitation to global warming. *J. Atmos. Sci.*, **68**, 123–138, doi:10.1175/2010JAS3542.1.
- Sherwood, S. C., W. Ingram, Y. Tsushima, M. Satoh, M. Roberts, P. L. Vidale, and P. A. O’Gorman, 2010: Relative humidity changes in a warmer climate. *J. Geophys. Res.*, **115**, D09104, doi:10.1029/2009JD012585.
- Singh, M. S., and P. A. O’Gorman, 2014: Influence of microphysics on the scaling of precipitation extremes with temperature. *Geophys. Res. Lett.*, **41**, 6037–6044, doi:10.1002/2014GL061222.
- , and —, 2015: Increases in moist-convective updraught velocities with warming in radiative-convective equilibrium. *Quart. J. Roy. Meteor. Soc.*, **141**, 2828–2838, doi:10.1002/qj.2567.
- Stein, T. H. M., R. J. Hogan, P. A. Clark, C. E. Halliwell, K. E. Hanley, H. W. Lean, J. C. Nicol, and R. S. Plant, 2015: The DYMECS Project: A statistical approach for the evaluation of convective storms in high-resolution NWP models. *Bull. Amer. Meteor. Soc.*, **96**, 939–951, doi:10.1175/BAMS-D-13-00279.1.
- Trenberth, K. E., A. Dai, R. Rasmussen, and D. Parsons, 2003: The changing character of precipitation. *Bull. Amer. Meteor. Soc.*, **84**, 1205–1217, doi:10.1175/BAMS-84-9-1205.
- van Meijgaard, E., L. H. Van Ulft, W. J. Van de Berg, F. C. Bosveld, B. J. J. M. Van den Hurk, G. Lenderink, and A. P. Siebesma, 2008: The KNMI regional atmospheric climate model RACMO version 2.1. KNMI Tech. Rep. 302, 43 pp. [Available online at [bibliotheek.knmi.nl/knmipubTR/TR302.pdf](http://bibliotheek.knmi.nl/knmipubTR/TR302.pdf).]
- Westra, S., and Coauthors, 2014: Future changes to the intensity and frequency of short-duration extreme rainfall. *Rev. Geophys.*, **52**, 522–555, doi:10.1002/2014RG000464.